J Therm Anal Calorim (2010) 99:385–390
DOI 10.1007/s10973-009-0380-1

The role of citrate precursors on the morphology of lanthanide oxides obtained by thermal decomposition

Mauro Francisco Pinheiro da Silva · Flávio Machado de Souza Carvalho · Tereza da Silva Martins · Márcia Carvalho de Abreu Fantini · Paulo Celso Isolani

Received: 26 February 2009 / Accepted: 22 July 2009 / Published online: 28 August 2009

Abstract Two series of lanthanide oxides with different morphologies were synthesized through calcinations of two types of citrate polymeric precursors. These oxides were characterized by XRD patterns, SEM electronic microscopy, and N_2 adsorption isotherms. SEM microscopy analysis showed that the calcination of crystalline fibrous precursors $[Ln_2(LH)_3{\cdot}2H_2O]$ (L = citrate) originated fibrous shaped particles. On the other hand, the calcination of irregular shaped particles of precursors $[LnL{\cdot}xH_2O]$ originated irregular shaped particles of oxide, pointing out a morphological template effect of precursors on the formation of the respective oxides.

Keywords Lanthanide oxides · Oxide morphologies · Polymeric precursors · SEM analysis

M. F. P. da Silva · P. C. Isolani (✉)
Instituto de Química, Universidade de São Paulo, CP 26077, Sao Paulo, SP 05513-970, Brazil
e-mail: pcisolan@iq.usp.br

T. da Silva Martins
Departamento de Ciências Exatas e da Terra, Universidade Federal de São Paulo, Sao Paulo, SP, Brazil

F. M. de Souza Carvalho
Instituto de Geociências, Universidade de São Paulo, Sao Paulo, SP, Brazil

M. C. de Abreu Fantini
Departamento de Física Aplicada, Instituto de Física, Universidade de São Paulo, Sao Paulo, SP, Brazil

Introduction

Materials designing on a nanometer scale remain still a challenge on chemistry and materials science [1–4]. The increasing necessity for nanostructured materials is a consequence of the demand for smaller and more efficient device building [5] among other high technology applications [6, 7] and academic investigations [8, 9].

On this way, lanthanide oxides-based and doped nanoparticles represent an interesting investigation field. On optical displays, for instance, europium oxide is utilized on visible light phosphors [10], catalysts and supports for noble metal catalysts [11]. Lanthanum oxide finds applications on solid oxide fuel cells [12]. CeO_2 is utilized as on three-way catalysts as oxygen storage for automotive pollution abatements [13].

Lanthanide oxides can be synthesized in several ways such as: sol–gel [14], hydrothermal [15], carbonate [16], templates [17], spray pyrolysis [18], homogeneous precipitation [19], alumina template [20] thermal treatment of polymeric precursors [21, 22], Pechini's method [23], reverse micellar system [24], and solvothermal methods [25]. Among them, the polymeric precursor method is very attractive, since it consists of a moderate temperature calcination of lanthanide organic polyacid salts, yielding high purity oxides. Besides its low cost, this method can be applied on large scale preparations due to its simplicity.

Recently, synthetic methods for achieving oxides with specific morphologies have been reported [26, 27] and consequently these oxide-based materials with characterized morphologies have been exploited as catalysts [28], phosphors [29], electrochemical electrode coatings [30], and thermoelectric applications [31].

Despite the amount of work on this subject, correlations between molecular properties of a solid precursor and

oxide morphology are still an open field of investigation. Few studies point out its importance [32–34].

This study shows a correlation between the characteristics of two citrate precursors (crystalline and amorphous) and the morphology of lanthanide oxides obtained by calcination.

Experimental

Syntheses

Lanthanide citrates [LnL·xH_2O] and [$Ln_2(LH)_3$·$2H_2O$], L = $(C_6H_5O_7)^{3-}$ and LH = $(C_6H_6O_7)^{2-}$ were synthesized following procedures already published [32]. These salts were named, respectively, precursor type 1 and 2. Calcination of the two precursors yielded, respectively, oxides type 1 and 2. These syntheses were carried out by heating ca. 1 g of precursor's type 1 and 2 simultaneously in a furnace, EDG mod. 3 P-S, under 50 mL min^{-1} air flux using a heating program of 10 °C min^{-1} up to 100 °C above the temperature of the last decomposition event determined by TG/DTG/DTA analyses [32], considering the respective phase diagrams for oxides formation [37, 38] (Table 1). All samples were kept at that temperature for 1 hour and left to cool down to room temperature in a desiccator, under anhydrous $CaCl_2$.

Characterizations

Precursor characterizations were reported previously [32]. Lanthanide oxides were characterized by X-ray diffraction patterns (XRD), BET multipoint surface analysis and scanning electron microscopy (SEM). XRD patterns of precursors were collected in $\theta/2\theta$ geometry between 10° and 90°; counting times were 2 s per point for a step size of 0.05° − 2θ, using Cu Kα (λ = 0.1518 nm) monochromatic radiation, operating at I = 20 mA, V = 40 kV. The Y_2O_3 standard was prepared by heating 99.99% purity Y_2O_3 (Aldrich) up to 1,200 °C. That temperature was maintained during 72 h, followed by slow cooling to room temperature for 36 h prior to the analyses. The XRD pattern of Y_2O_3 was collected in a $\theta/2\theta$ geometry between 5° and 120°, counting time 5 s per point, for a step size of 0.02° − 2θ. Calculations of oxide crystallite size from XRD patterns were performed through a Rietveld GSAS refining program [33–35]. Raman spectra of CeO_2 samples were recorded on a Renishaw mod. 3000 imaging system coupled to a He–Ne laser (Spectra Physics mod. 127, λ = 632.8 nm) equipped with an Olympus metallurgical microscope and a CCD detector. Crystallite size calculations through Raman spectroscopy were carried out by the phonon confinement model approach [36]. SEM images were recorded on a JEOL Field Emission Scanning Electron Microscope, JSM 7401F using a LEI detector. Oxide samples were previously recovered with 3 nm Au on an Edwards Scancoat operating at 15 mA and 1.5 kV. Surface area measurements were carried out on a Quantachrome analyzer NOVA 1200 e. Prior to surface area measurements, oxide samples were degassed at 300 °C under vacuum during 3 h. Surface areas were measured by N_2 adsorption at 77 K.

Table 1 Temperatures used for the synthesis of each pair of lanthanide oxides

Oxide	Temperature/°C
La_2O_3	900
CeO_2	600
Pr_6O_{11}	800
Nd_2O_3	750
Sm_2O_3	900
Eu_2O_3	900

Results

Oxide series types 1 and 2 were prepared by calcining precursors type 1, [LnL·xH_2O], and type 2, [$Ln_2(LH)_3$·$2H_2O$]. XRD patterns of these oxides are shown in Fig. 1. Analysis of these patterns showed that, except for neodymium oxides, all products were composed by only one crystallographic phase.

La_2O_3 obtained from both precursor types were identified as hexagonal A phase with P-3m1 space group (PDF#05-0602). CeO_2 and Pr_6O_{11} showed a cubic fluorite structure with Fm3m space group, respectively (PDF#34-0394), and (PDF#42-1121). Sm_2O_3 and Eu_2O_3 showed sesquioxide cubic C phases with IA3 space group, respectively (PDF#42-1461), and (PDF#43-1008). Nd_2O_3 obtained from both precursors showed different proportions of two phases: a sesquioxide P-3m1 hexagonal A phase (PDF#41-1089) and a sesquioxide IA3 cubic C phase (PDF#21-0579).

The phase diagram of lanthanide oxides has been determined by Tranverse [37, 38]. According to that the temperature used in La_2O_3 synthesis allows only the A phase stabilization. Both Nd_2O_3 types presented two phases (hexagonal A phase and cubic C phase). Rietveld XRD phase quantification analysis of both types show that type 1 is composed by approximately 59% of cubic phase and 41% of hexagonal phase. On the other hand, Nd_2O_3 type 2 is composed by 64% of hexagonal phase and 36% of cubic phase. Considering that the oxide with larger surface area

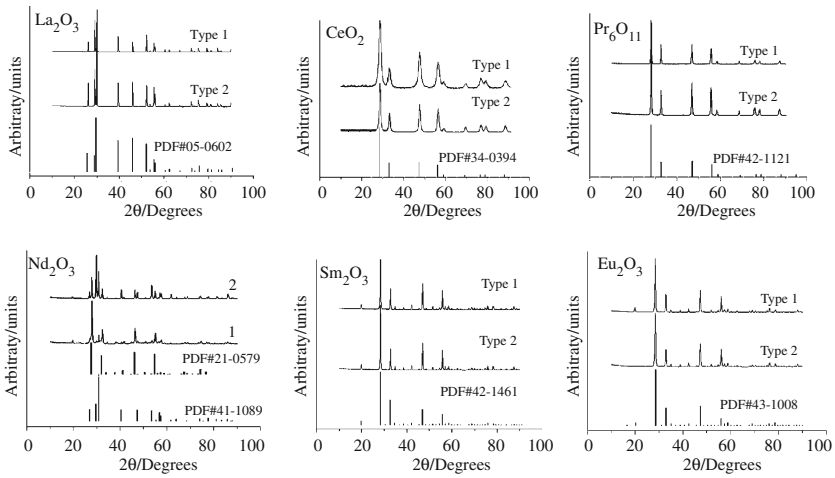

Fig. 1 XRD patterns of all synthesized oxides and line identifications

Table 2 Crystallographic, structural data, and surface areas of Lanthanide oxides

	Oxide Type	Space Group	Cell Type	Structure Type	Crystallite Size/nm	BET/m^2 g^{-1}
La_2O_3	1	P3m1	h	Sesq. A	>100	8
	2	P3m1	h	Sesq. A	>100	5
CeO_2	1	Fm3m	c	Fluorite	20	37
	2	Fm3m	c	Fluorite	21	19
Pr_6O_{11}	1	Fm3m	c	Fluorite	35	24
	2	Fm3m	c	Fluorite	43	10
Nd_2O_3	1	IA3	c	Sesq. C	36	19
		P3m1	h	Sesq. A	35	
	2	IA3	c	Sesq. C	>100	8
		P3m1	h	Sesq. A	68	
Sm_2O_3	1	IA3	c	Sesq. C	68	36
	2	IA3	c	Sesq. C	66	8
Eu_2O_3	1	IA3	c	Sesq. C	40	25
	2	IA3	c	Sesq. C	61	8

has the larger cooling rate, the difference in the compositions of two type of neodymium oxides were attributed to different cooling rates as a consequence of their different surface areas. The temperatures utilized for Sm_2O_3 and Eu_2O_3 syntheses are high enough for the formation of cubic C phase only. In the synthesis of CeO_2 and Pr_6O_{11}, the low oxidation potentials of Ce^{3+} and Pr^{3+} (3+ to 4+) made them to form cubic fluorite phases. Additionally, Rietveld XRD analysis of neodymium oxides type 2 showed also a preferential orientation along the (001) Miller direction of the hexagonal phase. Selected crystallographic data and results of average crystallite size calculations of all synthesized oxides are shown in Table 2.

Raman spectra of CeO_2 are shown in Fig. 2. One can observe the first order Raman active mode of CeO_2 at $\sim$465 cm^{-1} attributed to the triply degenerated symmetrical stretching vibration of the CeO_8 vibrational unit pointing out the fluorite structure of these oxides [39]. This vibration was used for all crystallite size calculations. Its FWHM, fitted by Lorentzian function, followed the sequence CeO_2 (1) > CeO_2 (2) varying inversely with crystallite size, as discussed above. Comparison of crystallite size between CeO_2 1 and 2 is shown in Fig. 2.

XRD and Raman spectroscopy crystallite size calculations are in reasonable agreement. Average crystallite size calculations through XRD patterns yielded, respectively, 20 and 21 nm for oxides type 1 and 2. Raman spectroscopy yielded 16 and 20 nm for oxides type 1 and 2. Due to the fact that the phonon confinement model is valid in the range of 20–50 nm crystallite size, our calculation has used this model on its borderline region, explaining this difference in the values obtained for type 1 [40]. XRD and Raman data do not suggest any meaning precursor influence on average crystallite size.

N_2 adsorption isotherms could be classified as Brunauer type III, evidencing the non-porous character of all oxides

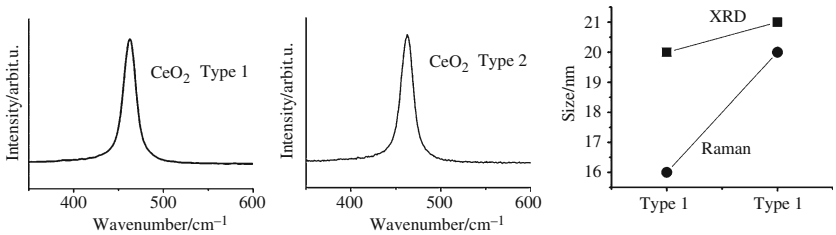

Fig. 2 Raman spectra of CeO_2 types 1 and 2. Comparison of CeO_2 crystallite size determinations from Raman spectroscopy and XRD patterns

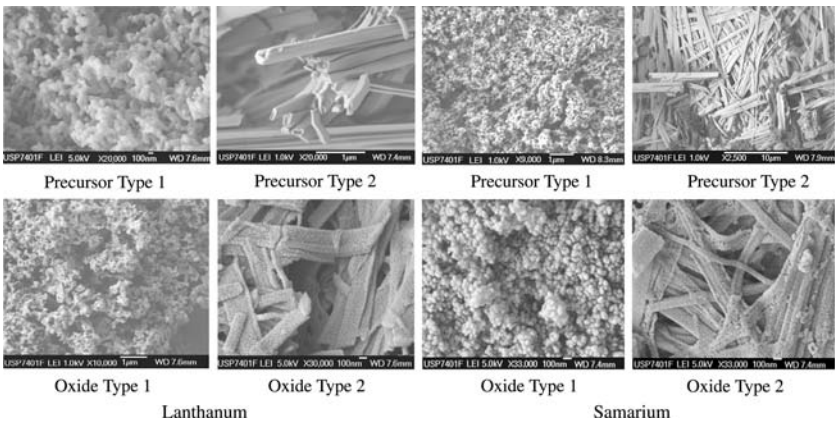

Fig. 3 SEM images of precursors and oxides types 1 and 2 of lanthanum and samarium

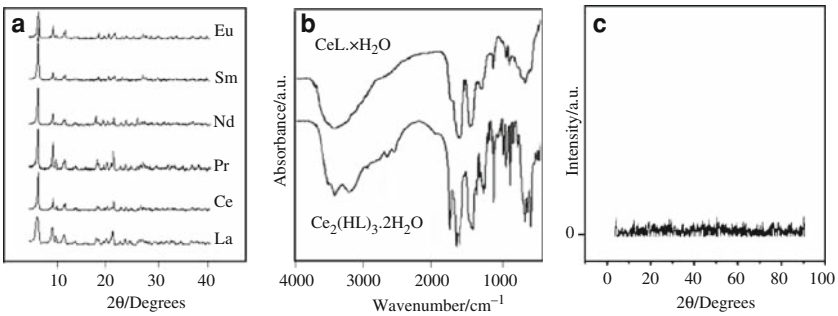

Fig. 4 **a** XRD patterns of precursors $[Ln_2(LH)_3{\cdot}2H_2O]$ (Ln = La–Eu). **b** FTIR spectra of $[CeL{\cdot}xH_2O]$ and $[Ce_2(LH)_3{\cdot}2H_2O]$. **c** XRD pattern of amorphous $[CeL{\cdot}xH_2O]$ (background subtracted)

of both series [41]. BET surface area analyses of these oxides are presented in Table 2. These analyses point out the striking morphological differences between these two oxide series. Systematically, type 1 oxides showed larger surface areas than oxides type 2. Considering that the calculated average crystallite sizes of both oxide types are approximately the same, for each pair, the surface area differences must be due to morphological differences.

SEM images of representative precursors type 1, $[LaL{\cdot}xH_2O]$ and $[SmL{\cdot}xH_2O]$ and precursors type 2 $[La_2(HL)_3{\cdot}2H_2O]$ and $[Sm_2(HL)_3{\cdot}2H_2O]$, and their respective oxides are shown in Fig. 3. These images show that precursors type 1 are composed by irregularly shaped particles and precursors type 2 are composed by fibrous particles. Figure 4 shows XRD analysis of all precursors type 2 and infrared spectra of two cerium citrates, as representative of the series [32]. These analyses evidence the crystalline character of precursors type 2 and amorphous character of precursors type 1 (including infrared broad bands in the latter).

SEM images of oxides obtained by calcination of precursors type 1 and 2 show that the initial morphologies of the respective precursors are held on the oxide particles. So, oxides type 1 presented irregularly shaped particles and oxides type 2 presented fibrous shaped particles. These data suggest strongly that the crystalline habit of precursor type 2 acts as a template, driving the formation of morphology of the corresponding oxide, yielding fiber shaped particles. On the same way, the irregularly shaped aggregates of precursors type 1 drive the formation of particles of oxides type 1, yielding irregular particles. This behavior was observed on the synthesis of all lanthanide oxides (La through Eu).

Conclusions

Two series of lanthanide oxides with different morphologies were synthesized and characterized. Clear dependence between morphologies of oxide and precursors are evidenced by SEM images. The fibrous character of precursor type 2 and irregular particles of precursor type 1 are held during calcination and, consequently, the respective oxides present similar morphologies. The present study points out the template effect of precursor morphology during the syntheses of lanthanide oxides through thermal decomposition of lanthanide citrates. Investigations of catalytic properties of these two oxide series are under way in our laboratory.

Acknowledgements MFPS thanks CAPES (Brazil) for a doctoral fellowship. We thank Márcia L. A.Temperini, Renato S. Freire (IQ-USP), Marilda M. G. R. Vianna, and Maria L. P. da Silva (EP-USP). We thank also FAPESP (grant 05/02745-7) for the BET equipment.

References

1. Cansell F, Aymonier CJ. Design of functional nanostructured materials using supercritical fluids. J Supercrit Fluids. 2009;47: 508–16.
2. Lee JH, Wang ZM, Abu-Waar ZY, Salamo GJ. Design of nanostructure complexes by droplet epitaxy. Cryst Growth Des. 2009;9:715–21.
3. Zhang G, Wang W, Lu X, Li X. Solvothermal synthesis of V–VI binary and ternary hexagonal platelets: the oriented attachment mechanism. Cryst Growth Des. 2009;9:145–50.
4. Qian L, Zhu J, Chen Z, Gui Y, Gong Q, Yuan Y, et al. Graphical abstract. Eur J Chem. 2009;15:12–33.
5. Rolison DR, Long JW, Lytle JC, Fischer AE, Rhodes CP, Mc Evoy TM, et al. Multifunctional 3D nanoarchitectures for energy storage and conversion. Chem Soc Rev. 2009;38:226–52.
6. Laurence TA, Braun G, Talley C, Schwartzberg A, Moskovits M, Reich N, et al. Rapid, solution-based characterization of optimized SERS nanoparticle Substrates. J Am Chem Soc. 2009;131:162–9.
7. Qiu H, Yang J, Kodali P, Koh J, Ameer GA. A citric acid based hydroxyapatite composite for orthopedic implants. Biomaterials. 2007;28:5845–54.
8. Deshpande AC, Singh SB, Abyaneh MK, Pasricha R, Kulkarni SK. Low temperature synthesis of ZnSe nanoparticles. Mater Lett. 2008;62:3803–5.
9. Papadimitriou S, Tegou A, Pavlidou E, Armyanov S, Valova E, Kokkinidis G, et al. Preparation and characterisation of platinum- and gold-coated copper, iron, cobalt and nickel deposits on glassy carbon substrates. Electrochim Acta. 2008;53:6559–67.
10. Chawla S, Kumar N, Chander H. Optical properties of nanocrystalline-coated Y_2O_3:Er^{3+}, Yb^{3+} obtained by mechanochemical and combustion synthesis. J Lumin. 2009;129:114–8.
11. Guo Y, Lu G, Zhang Z, Zhang S, Qi Y, Liu Y. Preparation of $Ce_xZr_{1-x}O_2$ ($x = 0.75, 0.62$) solid solution and its application in Pd-only three-way catalysts. Catal Today. 2007;126:296–302.
12. Tok AIY, Boey FYC, Dong Z, Sun XL. Hydrothermal synthesis of CeO2 nano-particles. J Mater Process Technol. 2007;190:217–22.
13. Kuang Q, Lin Z, Lian W, Jiang Z, Xie Z, Huang R, et al. Syntheses of rare-earth metal oxide nanotubes by the sol–gel method assisted with porous anodic aluminum oxide templates. J Solid State Chem. 2007;180:1236–42.
14. Liu Q, Luo L. Preparation and luminescent properties of Eu-doped Ln_2O_3 (Ln = Gd, Lu) thin film by citrate sol–gel process. Ceram Int. 2004;3:1703–6.
15. Zhao Y, Frost RL, Vagvolgyi V, Waclawik ER, Kristof J, Horvath E. XRD, TEM and thermal analysis of yttrium doped boehmite nanofibres and nanosheets. J Therm Anal Calorim. 2008;94:219–26.
16. Panchula ML, Akinc M. Morphology of lanthanum carbonate particles prepared by homogeneous precipitation. J Eur Ceram Soc. 1996;16:833–41.
17. Piegza J, Zych E, Hreniak D, Strek W, Kepinski L. Structural and spectroscopic characterization of Lu_2O_3:Eu nanocrystalline spherical particles. J Phys Condens Matter. 2004;16:6983–94.
18. La R, Hu Z, Li H, Shang X, Yang Y. Synthesis and morphological control of rare earth oxide nanoparticles by solvothermal reaction. Mater Sci Eng. 2004;368:145–8.
19. Elbaccouch MM, Shukla S, Mohajeri N, Seal S, Raissi AT. Microstructural analysis of doped-strontium cerate thin film membranes fabricated via polymer precursor technique. Solid State Ionics. 2007;178:19–28.
20. Santos SF, de Andrade MC, Sampaio JA, da Luz AB, Ogasawara T. Synthesis of ceria-praseodymia pigments by citrate-gel method for dental restorations. Dyes Pigments. 2007;75:574–9.
21. Pires AM, Serra OA, Davolos MR. Morphological and luminescent studies on nanosized Er, Yb–Yttrium oxide up-converter prepared from different precursors. J Lumin. 2005;113:174–82.
22. Yin S, Aita Y, Komatsu M, Wang J, Tang Q, Sato T. Synthesis of excellent visible-light responsive $TiO_{2-x}N_y$ photocatalyst by a homogeneous precipitation-solvothermal process. J Mater Chem. 2005;15:674–82.
23. Pechini MU. US Patent no 3330697; 1967.
24. Frías D, Nousir S, Barrio I, Montes M, López T, Centeno MA, et al. Synthesis and characterization of cryptomelane- and birnessite-type oxides: precursor effect. Mater Charact. 2007;58: 776–81.
25. Yin S, Akita M, Shinozaki R, Li T, Sato J. Synthesis and morphological control of rare earth oxide nanoparticles by solvothermal reaction. J Mater Sci. 2008;43:2234–9.
26. Počuča M, Branković G, Branković Z, Vasiljević-Radović D, Mitrić JM. Tailoring of morphology and orientation of $LaNiO_3$ films from polymeric precursors. Eur Ceram Soc. 2007;27: 3819–22.
27. Mandal S, Müller AHE. Facile route to the synthesis of porous α-Fe_2O_3 nanorods. Mater Chem Phys. 2008;111:438–43.
28. Ntainjua ENT, Garcia B, Solsona S, Taylor H. The influence of cerium to urea preparation ratio of nanocrystalline ceria catalysts for the total oxidation of naphthalene. Catal Today. 2008;137: 373–8.
29. Kubrin R, Bauhofer W. Influence of polymeric additives on morphology and performance of Y_2O_3:Eu phosphor synthesized by flame-assisted spray pyrolysis. J Lumin. 2009;129:1060–6.
30. Jia Z, Yue L, Zheng Y, Xu Z. The convenient preparation of porous CuO via copper oxalate precursor. Mater Res Bull. 2008;43:2434–40.
31. Zhang X, Ding Y, Zhang Y, Hao Y, Meng G, Zhang L. Thermal behavior of antimony nanowire arrays embedded in anodic aluminum oxide template. J Therm Anal Calorim. 2007;89:493–7.
32. Da Silva MFP, Matos JR, Isolani PC. Synthesis, characterization and thermal analysis of 1:1 and 2:3 lanthanide(III) citrates. J Therm Anal Calorim. 2008;94:305–11.
33. Paraschiv C, Jurca B, Ianculescu AO. Synthesis of nanosized bismuth ferrite ($BiFeO_3$) by a combustion method starting from $Fe(NO_3)_3{\cdot}9H_2O$-$Bi(NO_3)_3{\cdot}9H_2O$-glycine or urea systems. J Therm Anal Calorim. 2008;94:411–6.

34. Toby BH. EXPGUI, a graphical user interface for GSAS. J Appl Crystallogr. 2001;34:210–3.
35. Larson AC, Von Dreele RB. GSAS: general structural analysis system. Los Alamos, NM: Los Alamos National Laboratory; 1994.
36. Kosacki I, Suzuki T, Petrovsky V, Anderson HU, Colomban PH. Raman scattering and lattice defects in nanocrystalline CeO_2 thin films. Solid State Ionics. 2002;149:99–105.
37. Foex M, Traverse JP. Remarques sur les Transformations Cristallines Presentees & Haute Temperature par les Sesquioxydes de Terres Rares. Rev Int Hautes Temp Refract. 1966;3:429–53.
38. Foex M, Traverse JP. Remarques sur les Transformations Cristallines Presentees & Haute Temperature. Bull Soc Fr Mineral Crystallogr. 1966;89:184–201.
39. Trovarelli A, Zamar F, Llorca J, de-Leitenburg C, Dolcetti G, Kiss JT. Nanophase fluorite-structured CeO_2–ZrO_2 catalysts prepared by high-energy mechanical milling. J Catal. 1997;169:490–502.
40. Siu GG, Stokes MJ, Liu Y. Variation of fundamental and higher-order Raman spectra of ZrO_2 nanograins with annealing temperature. Phys Rev B. 1999;59:3173–9.
41. Brunauer S, Deming LS, Deming WS, Teller E. On a theory of the van der Waals adsorption of gases. J Am Chem Soc. 1940;62:1723–32.